Metal-chalcogen bond-length induced electronic phase transition from semiconductor to topological semimetal in ZrX$_2$ (X=Se and Te)

Indrani Kar,[1] Joydeep Chatterjee,[1] Luminita Harnagea,[2] Y. Kushnirenko,[3] A. V. Fedorov,[3] Deepika Shrivastava,[1] B. Büchner,[3] P. Mahadevan,[1] and S. Thirupathaiah[1,3,*]

[1]*Condensed Matter Physics and Material Sciences Department, S N Bose National Centre for Basic Sciences, Kolkata, West Bengal-700106, India*
[2]*Indian Institute of Science Education and Research, Dr. Homi Bhabha Road, Pune, Maharashtra-411008, India*
[3]*Leibniz Institute for Solid State Research, IFW Dresden, D-01171 Dresden, Germany*

Topological transition-metal dichalcogenides have been the center of research interests in materials science, recent days, due to their potential applications in spintronics, optoelectronics, and quantum computations. In this paper, using angle resolved photoemission spectroscopy (ARPES) and density functional theory (DFT) calculations, we systematically studied the low-energy electronic structure of bulk ZrTe$_2$. ARPES studies on ZrTe$_2$ demonstrate free charge carriers at the Fermi level, which is further confirmed by the DFT calculations. An equal hole and electron carrier density estimated from the ARPES data points to ZrTe$_2$ being a semimetal. The DFT calculations further suggest a band inversion between Te p and Zr d states at the Γ point, hinting at the nontrivial band topology in ZrTe$_2$. Thus our studies suggest that ZrTe$_2$ is a topological semimetal. Also, a comparative band structure study is done on ZrSe$_2$, which shows a semiconducting nature of the electronic structure with an indirect band gap of 0.9 eV between $\Gamma(A)$ and $M(L)$ high-symmetry points. Below we show that the metal-chalcogen bond length plays a critical role in the electronic phase transition from a semiconductor to a topological semimetal ingoing from ZrSe$_2$ to ZrTe$_2$.

I. INTRODUCTION

Transition metal dichalcogenides (TMDCs) [1–3] are gaining a great deal of research interests, especially, from the past few decades due to their potential applications in spintronics [4–8] and as well in the optoelectronics [9–13] because of their wide range of electronic properties starting from the metallic [14–16], to the semimetallic [17–20], to the semiconducting [21–24], and to the Mott insulators [25–27], obtained mainly by the band engineering [28–30]. In addition, the diversity of electronic properties of TMDCs includes the charge density wave (CDW) [31,32], the magnetism [33–35], and the superconductivity [36–38].

Tunable band gap in layered TMDCs is one of the major research topics in recent days from both the theory and experiment [39–42]. It is known that the band gap in IVB TMDCs (TiX_2, ZrX_2, and HfX_2, where X = S, Se, and Te) change with the strain [43]. However, among the IVB TMDCs, ZrX_2 compounds in their monolayer thickness show peculiarity beyond a critical pressure. That means, instead of increasing band gap with the increasing pressure, it starts decreasing beyond the critical pressure. On the other hand, the monolayer thickness ZrTe$_2$ transforms from metal to a semiconductor beyond a critical pressure. Hence, understanding the pressure effects on the electronic structure of TMDCs has a significance in

their band engineering [44]. Specifically, performing ARPES studies under external pressure is a nontrivial method [45,46]. However, studying the electronic structure using ARPES under the application of chemical pressure induced by the substitution of an isovalent atom is highly viable [47]. So far there exists very few ARPES reports in this direction [48–52]. Moreover, these studies report only the electronic structure of Zr(Se$_{1-x}$S$_x$)$_2$ which are semiconductors. Although several theoretical reports on ZrTe$_2$ predicted it to be a metal [53–55], so far no ARPES study exists on this compound in bulk phase confirming the same, except that a recent ARPES study on monolayer ZrTe$_2$ deposited on InAs (111) substrate showing linear Dirac states near the Fermi level at the Γ point [56]. Thus a thorough understanding of the electronic structure of bulk ZrTe$_2$ has interests from other reasons as well, whether ZrTe$_2$ is another topological system like ZrTe$_5$ [57–61]. Therefore ARPES studies on the bulk ZrTe$_2$ are essential to understand whether ZrTe$_2$ is a simple metal or a topological semimetal.

In this paper, we report on the low-energy electronic structure of bulk ZrTe$_2$ and ZrSe$_2$ using high-resolution angle resolved photoemission spectroscopy and density functional theory. On the Fermi surface map of ZrTe$_2$, we observe several well disconnected hole and electron pockets at $\Gamma(A)$ and $M(L)$ points, respectively. Further, in ZrTe$_2$, we realize three holelike nondegenerate band dispersions near the $\Gamma(A)$ point and an electronlike band dispersion at the $M(L)$. Our DFT calculations predict all hole pockets are composed by the Te p

*setti@bose.res.in
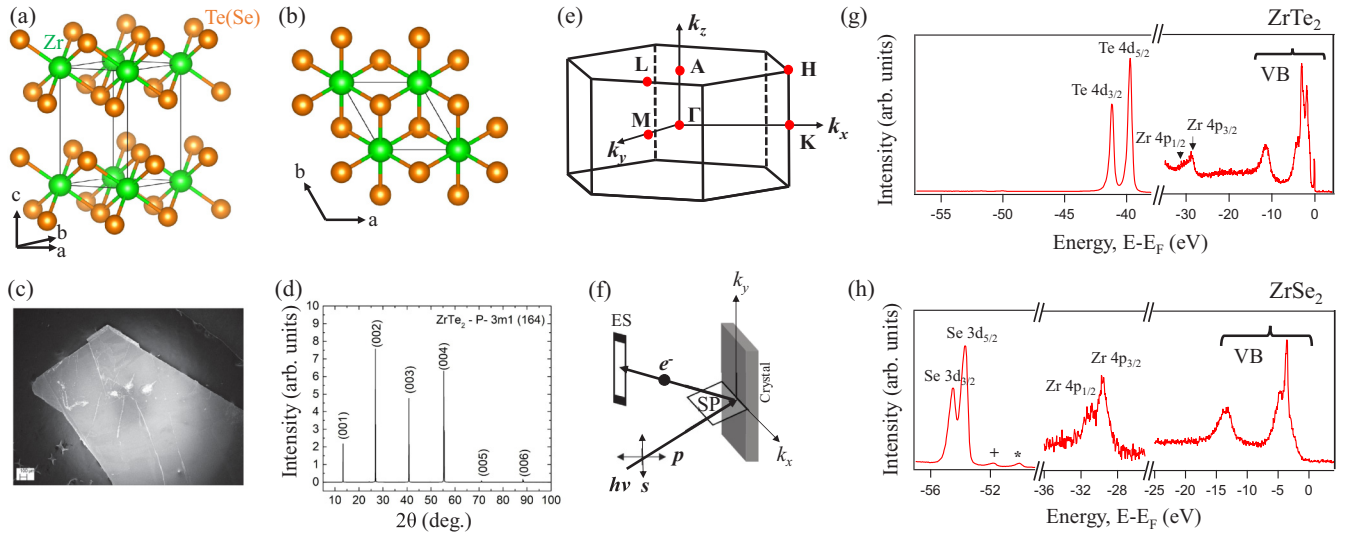
FIG. 1. (a) Trigonal crystal structure of $ZrTe_2$ and $ZrSe_2$. (b) ZrX_2 layer projected on the *ab*-plane, showing the metal-chalcogen hexagonal pattern. (c) Scanning electron microscope image of the $ZrTe_2$ single crystal with a spacial resolution of 100 μm. (d) X-ray diffractogram of $ZrTe_2$ single crystal. (e) 3D view of the hexagonal Brillouin zone with high-symmetry points. (f) Measuring geometry of photoemission spectroscopy, defining the *s*- and *p*-polarized photons with respect to the scattering plane (SP) and analyzer entrance slit (ES). Core level photoemission spectra of (g) $ZrTe_2$ and (h) $ZrSe_2$. In (h), the symbols + and ⋆ represent the iodine impurity peaks of $4p_{3/2}$ and $4p_{5/2}$, respectively.

orbital characters and the electron pocket is composed by the Zr d_{z^2} orbital character. An equal number of hole and electron carrier density estimated from our ARPES data using Luttinger's theorem [62,63] suggests $ZrTe_2$ to be a semimetal. In addition, our DFT calculations on $ZrTe_2$ in presence of spin-orbit coupling (SOC) predict band inversion between Te *p* and Zr *d* characters near Γ point, pointing $ZrTe_2$ to a topological semimetal. In contrast to $ZrTe_2$, from the Fermi surface topology of $ZrSe_2$, we observe only electron pockets located at the $M(L)$ point, while the hole pockets are noticed well below the Fermi level at a binding energy of ≈1 eV. Nevertheless, our studies on $ZrSe_2$ are inline with the existing reports that it is a semiconductor with an indirect band gap of 0.9 eV between Γ(A) and M(L) high-symmetry points [51,52,64]. In order to understand the origin of semimetallic state in $ZrTe_2$ and semiconducting state in $ZrSe_2$, we quantified the electronic structure by mapping it onto a tight-binding model. This allows us to relate the electronic structure changes in going from $ZrSe_2$ to $ZrTe_2$ to the change in the metal-chalcogen bond lengths. Further, by looking at other compounds in the same column of periodic table HfX_2, we conclude that a similar mechanism is operational for the Hf based compounds. Here again, the metal-chalcogen bond length dictates the nature of the underlying ground state, $HfSe_2$ is semiconducting while $HfTe_2$ is metallic.

II. EXPERIMENTAL DETAILS

High-quality single crystals of $ZrSe_2$ and $ZrTe_2$ were grown by the chemical vapor transport (CVT) technique using iodine as a transport agent [65]. In the first step, stoichiometric quantities of elements, Zr (sponge, 99.9%, metals basis, Sigma Aldrich) with Se (shot, Alfa Aesar, 99.999%, metals basis) or Te (ingot, 99.99%, metals basis, Alfa Aesar), were loaded into an alumina crucible and subsequently sealed in

a quartz ampoule under vacuum. The ampoule was slowly heated to 500 °C, with a rate of 50 °C/h, kept there for 5 h and then heated further to 900 °C. This temperature has been maintained for a period of 2 days, in order to complete the reaction between Zr and the chalcogen (Se/Te). The polycrystalline powders of $ZrSe_2$ and $ZrTe_2$ were used for the single crystal growth. The powdered samples were placed and sealed under vacuum in quartz ampoules together with pieces of crystallized iodine (5 mg/cm³). The ampoules had subsequently been loaded in a three-zone furnace, where a gradient of temperature of 100 °C was maintained between the source (880 °C) and the sink (780 °C) zone. After 10 days of transport, many single crystals with dimensions as large as 5 mm × 5 mm × 0.1 mm were obtained at the cold part of the ampoule. Crystal structure, morphology and chemical composition of the single crystals were determined using x-ray diffraction and scanning electron microscope equipped with an energy dispersive x-ray analysis probe (EDAX), see Fig. 1. From EDAX (see Ref. [66]), we further identify that the studied samples in this contribution have the chemical compositions of $Zr_{1.02}Se_2$ and $Zr_{1.16}Te_2$ with 2% and 16% excess Zr per formula unit, respectively. Both the compounds crystallized in the space group of P$\bar{3}$m1 (164), with lattice parameters at room temperature as *a* = *b* = 3.945 Å and *c* = 6.624 Å for $ZrTe_2$ and *a* = *b* = 3.766 Å and *c* = 6.150 Å for $ZrSe_2$.

Angle resolved photoemission spectroscopy measurements were carried out at the UE-112 beam-line equipped with 1³-ARPES end station located in BESSY II (Helmholtz zentrum Berlin) synchrotron radiation center [67,68]. Photon energies for the measurements were varied between 30 to 110 eV. The energy resolution was set between 10 and 15 meV depending on the excitation energy. Data were recorded at a chamber vacuum of the order of 1 × 10⁻¹⁰ mbar and the sample temperature was kept at 1 K during the measurements. We

employed various photon polarizations in order to extract the electronic structure comprehensively.

III. BAND STRUCTURE CALCULATIONS

The electronic structure of $ZrSe_2$ and $ZrTe_2$ have been calculated within a projected augmented plane wave (PAW) method of density functional theory as implemented in the Vienna *ab-initio* simulation package (VASP) [69,70]. A k mesh of $16 \times 16 \times 16$ was considered for the k-point integration while a plane-wave cutoff of 700 eV was used for the basis sets. The GGA-PBE approximation to the exchange correlation functional was used [71]. The experimental crystal structures were taken for the starting structural information. A full optimization of the lattice parameters as well as the internal positions was carried out. The optimized in-plane lattice parameter for $ZrSe_2$ was found to be $a = b = 3.735$ Å and that along the stacking direction $c = 6.206$ Å. Similarly for $ZrTe_2$, the optimized lattice parameters along the in-plane direction $a = b = 3.909$ Å and that along the stacking direction $c = 6.749$ Å were obtained. They represent about 1%–2 % deviations from the experimental values. In order to quantify the electronic structure changes between $ZrTe_2$ and $ZrSe_2$, we carried out a DFT band mapping onto a tight-binding model using the VASP to WANNIER90 interface [72,73], which had maximally localized Wannier function for the radial parts of the wave function. Zr d and Se/Te s and p states were included for the band mapping. Similar calculations are performed on $HfSe_2$ and $HfTe_2$. The structural parameters used for the calculations are given in Ref. [66].

IV. RESULTS

Figure 1(a) shows the trigonal crystal structure of ZrX_2. Figure 1(b) shows the projected Zr-chalcogen layer on the *ab* plane where one can notice each Zr ion is octahedrally coordinated with six Te (Se) ions. From the EDAX measurements on $ZrTe_2$ and $ZrSe_2$ (see Ref. [66]), we derived the chemical formulas of $Zr_{1.02}Se_2$ and $Zr_{1.16}Te_2$, respectively, suggesting that there is a 2% of Se (excess Zr) and a 16% of Te (excess Zr) deficiency from the stoichiometric compositions. Such a chalcogen deficiency or excess Zr in these systems generally leads to excess electron carrier density. Nevertheless, from our EDAX we noticed that the samples are homogeneous. As shown in Figs. 1(g) and 1(h), we performed x-ray photoemission spectroscopy (XPS) on $ZrTe_2$ and $ZrSe_2$, respectively. Most of the atomic core levels are assigned to their respective binding energies for $ZrTe_2$. However, for $ZrSe_2$, we noticed significant intensity peaks at binding energies of 52 and 50.6 eV, pointed by $+$ and $\star$, respectively, that are negligibly visible in $ZrTe_2$. These peaks are identified as the iodine $4p_{3/2}$ ($+$) and $4p_{5/2}$ ($\star$) states. Note here that iodine was used as a transport agent for growing these crystals, hence, some of the iodine atoms may have stuck in between the $ZrSe_2$ layers during the crystal growth process. But nevertheless, as we discuss below presence of Iodine in $ZrSe_2$ has no net effect on its electronic structure. Apart from this, we do not find any other impurity peaks from the XPS of $ZrSe_2$ and as well from $ZrTe_2$.
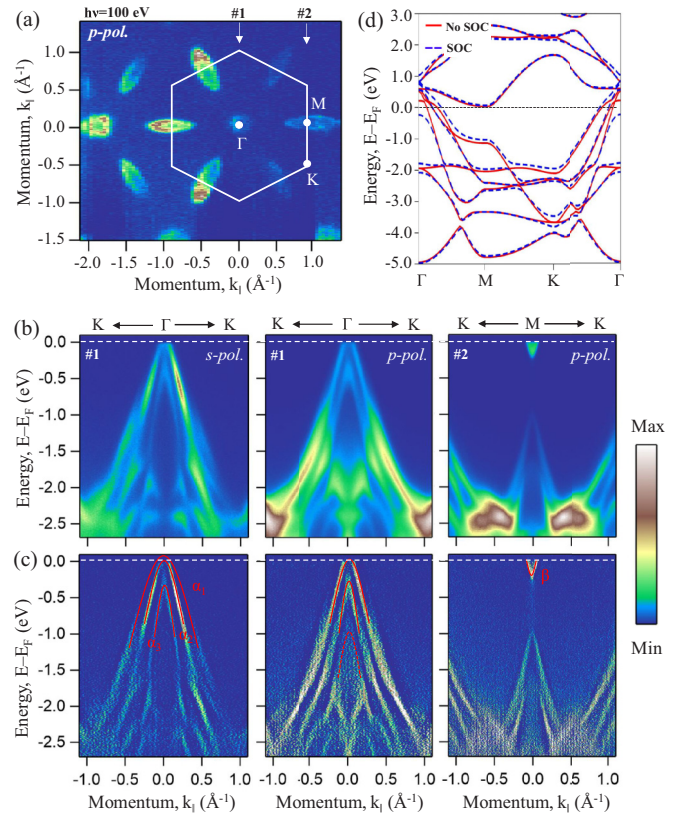
FIG. 2. In-plane electronic structure of $ZrTe_2$. (a) Fermi surface map measured using p polarized light with a photon energy hν = 100 eV. (b) Energy distribution maps (EDMs) taken along the cuts 1 and 2 as shown in (a). (c) Second derivatives of (b). In (c), the red-dashed curves are eye-guides showing the band dispersions. (d) Energy-momentum plot of $ZrTe_2$ calculated using density functional theory with (blue) and without (red) including spin-orbit coupling.

Figure 2 shows ARPES data of $ZrTe_2$. Fermi surface map of $ZrTe_2$ in the k_x-k_y plane is shown in Fig. 2(a), measured with p-polarized light using a photon energy of hν = 100 eV. The Fermi surface has hexagonal symmetry which is consistent with the hexagonal crystal structure. As can be observed in Fig. 2(a) the Fermi surface of $ZrTe_2$ consists of well disconnected Fermi pockets located at the Γ and M points. In order to understand nature of these Fermi pockets, we have taken the energy distribution maps (EDMs) along cuts 1 and 2 as shown in Fig. 2(a). From the EDMs shown in Fig. 2(b), three holelike band dispersions, α_1, α_2, and α_3, are found at $\Gamma(A)$ and an electronlike band dispersion, β, is found at $M(L)$ high-symmetry points. From the polarization dependent EDMs as shown in Fig. 2(b), with s-polarized light we noticed all three hole pockets with reduced intensity for α_1 and α_3 and high intensity for α_2, whereas with p-polarized light we noticed predominantly two hole pockets (α_2 and α_3). Our orbital resolved band structure (see Fig. 6 and Fig. S3 in Ref. [66]) in the absence of SOC suggest that the hole pocket α_1 is composed by Te p_x, the hole pocket α_2 is composed by Te p_y, and the hole pocket α_3 is composed by Te p_z character. However, in the presence of SOC the orbital contribution to the hole pockets is more complex as
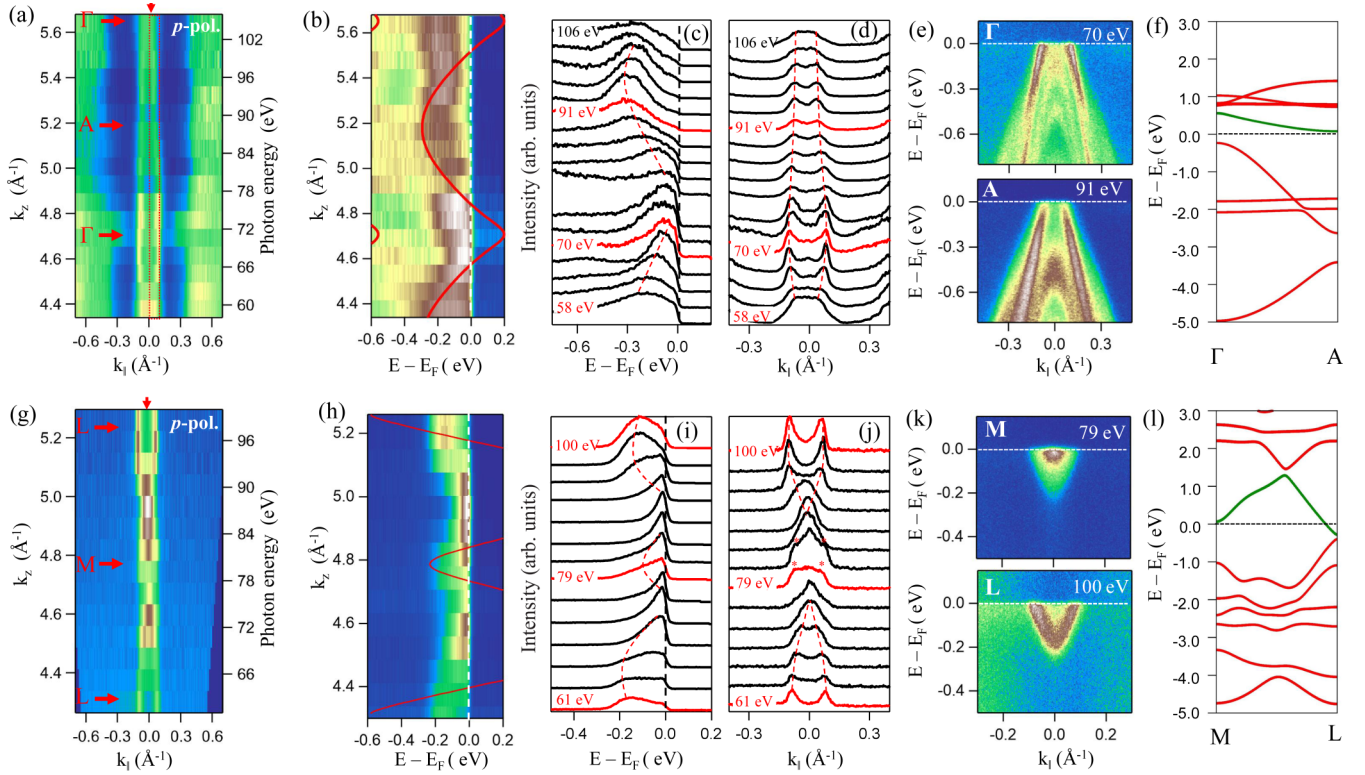
FIG. 3. Out-of-plane (k_z) electronic structure of ZrTe$_2$. (a) k_z Fermi surface map measured using p-polarized light in the ΓMAL plane. (b) EDM taken along the Γ- A high-symmetry line. (c) Photon energy dependent EDC curves extracted from (b). (d) Photon energy dependent MDC curves extracted from (a). (e) EDMs taken from Γ and A high-symmetry points. (f) Energy-momentum plot from the calculations along the Γ-A high-symmetry line. (g) k_z Fermi surface map measured using p-polarized light in the $MKHL$ plane. (h) EDM taken along the M-L high-symmetry line. (i) Photon energy dependent EDC curves extracted from (h). (j) Photon energy dependent MDC curves extracted from (g). (k) EDMs taken from M and L high-symmetry points. (l) Energy-momentum plot from the calculations along the M-L high-symmetry line. In (b) and (h) the DFT band structures along Γ-A and M-L are overlapped on the ARPES data by shifting the calculated Fermi level 0.3 eV towards lower binding energy. Note that since the band renormalization effects are not consider, only a qualitative agreement is found between theory and experiment.

can be observed in Fig. 6. Thus assigning orbital characters to the experimental band structure for ZrTe$_2$ is nontrivial. Next, an high-intense electron pocket (β) has been recorded using p-polarized light which is composed by the even parity orbital Zr d_{z^2} character. Figure 2(d) shows calculated band structure with and without including spin-orbit coupling. As we can be see from Fig. 2(d), three holelike and an electronlike band dispersions are predicted at $\Gamma(A)$ and $M(L)$ high-symmetry points. Therefore calculated band structure is qualitatively in agreement with the experimental data.

Despite being a layered system, we further performed photon energy dependent ARPES measurements on ZrTe$_2$ to unravel the out-of-plane (k_z) band structure. Figure 3(a) shows Fermi surface map of ZrTe$_2$ in the ΓMLA plane measured with photon energies ranging from 58 to 106 eV in step of 3 eV using p-polarized light. Following the equation, $k_z = \sqrt{\frac{2m}{\hbar^2}} \sqrt{V_0 + E_k \cos^2 \theta}$, here m is the electron mass, $\hbar$ is the Planck's constant, E_k is the photoelectron kinetic energy, θ is escape angle of the photoelectron from the sample surface normal, and V_0 is the inner potential of the sample which is considered to be 16 eV, we found that the photon energies 70 ± 3 and 91 ± 3 eV correspond to the high-symmetry points of Γ and A, respectively. Figure 3(b) shows EDM taken along

the Γ-A direction as shown by the down arrow in Fig. 3(a) extracted by a momentum integration of 0.05 Å^{-1}. From this EDM one can clearly notice that there is significant k_z dispersion ingoing from Γ to A for the hole pocket which has a partial contribution from Zr d_{z^2} along with Te $p_x(p_y)$ under SOC [see Fig. 6]. This is further demonstrated using photon energy dependent EDCs as shown in Fig. 3(c). Figure 3(d) shows photon energy dependent momentum dispersive curves (MDCs) extracted from Fig. 3(a). We estimated a Fermi vector of hole pocket $k_F \approx 0.09$ Å^{-1} at the Γ-point, while a Fermi vector $k_F \approx 0.06$ Å^{-1} is estimated at the A point. This observation again confirms significant k_z dispersion of the hole pocket. Figure 3(e) shows EDMs from Γ (70 eV) and A (91 eV) high-symmetry points. This observation is consistent with our DFT calculations along Γ-A direction as shown in Fig. 3(f), where one can see a significant k_z dispersion for the hole pocket (green color band dispersion).

Similarly, Figure 3(g) shows k_z Fermi surface map in the $MKHL$ plane measured with photon energies ranging from 61 to 100 eV in step of 3 eV using p-polarized light. From these data, we found that the photon energy 79 eV detects bands from the M point, whereas the photon energies 61 and 100 eV detect the bands from the L point. Figure 3(h) shows EDM along the M-L orientation and Fig. 3(i) shows photon

energy dependent EDCs taken from Fig. 3(h). Figure 3(j) shows photon energy dependent MDCs. We estimate a Fermi vector $k_F \approx 0.08$ Å^{-1} for the electron pocket at the L point, while no Fermi vector for the electron pocket is found at the M point. This observation is suggesting that the k_z dispersion of the electron pocket composed by Zr d$_{z^2}$ orbital character is relatively stronger. Further, in Fig. 3(j), we could identify a couple of peaks shown by ⋆ symbol on the MDC curves taken around the M point. These peaks are caused by the reminiscent spectral intensity of the electron pocket from the L point. This is because, in ARPES the photon energy dependent data generally suffer from the k_z resolution due to vertical transition of the photoelectrons. Thus the k_z dependent ARPES data generally consist of overlapping states in the k_z direction. Figure 3(k) shows EDMs from M (79±3 eV) and L (100±3 eV) high-symmetry points. This observation is consistent with our DFT calculations along M-L direction as shown in Fig. 3(l), where one can see a significant k_z dispersion for the electron pocket (green color band dispersion).

Next, ARPES data of ZrSe$_2$ are shown in Fig. 4. Figure 4(a) shows the Fermi surface map measured with a photon energy of h$\nu = 100$ eV using p-polarized light in the k_x-k_y plane. Figure 4 (b) shows energy-momentum plot of ZrSe$_2$ from DFT calculations. On the Fermi surface, we could identify six Fermi pockets located at six $M(L)$ points in a hexagonal symmetry. On the other hand, we did not find any spectral intensity at the $\Gamma(A)$ point. To further elucidate the nature of the band dispersions at the $M(L)$ and $\Gamma(A)$ points, we measured energy distribution maps along the direction as shown in Fig. 4(a). Figures 4(c) and 4(d) are such EDMs measured with photon energy of h$\nu = 100$ eV using p- and s polarized lights, respectively. From these EDMs it is clear that there are three well resolved holelike band dispersions, α_1, α_2, and α_3, near the $\Gamma(A)$ point with the valance band top well below the Fermi level at a binding energy of $E_B \approx 1$ eV. Further, we found an electronlike band dispersion, β, crossing the Fermi level with a Fermi vector $k_F = 0.06$ Å^{-1} at the $M(L)$ point. This electron pocket is almost disappearing when measured with s-polarized light as shown in Fig. 4(d). The orbital resolved band structure of ZrSe$_2$ (see Fig. S4 in Ref. [66]) suggests that the holelike band dispersions are composed by Se p_x, p_y, and p_z orbital characters, while the electronlike band near the $M(L)$ point is composed by the Zr d$_{z^2}$ orbital character. Thus the electron pocket is more intense when measured using p-polarized light compared to s-polarized light as in the current measuring geometry near the Fermi level the p-polarized light detects predominantly even parity orbital characters like d_{z^2}, p_x and p_z whereas the s-polarized light detects p_y character. Figure 4(e) shows the sum of EDMs from Figs. 4(c) and 4(d). Figure 4(f) is the second derivative of Fig. 4(e). From Figs. 4(e) and 4(f), we estimated an indirect band gap of 0.9 eV between the top of holelike (valance) band, α_1, near the $\Gamma(A)$ point and the bottom of electronlike (conduction) band, β, near the $M(L)$ point. These observations are in good agreement with earlier ARPES studies on this system, i.e., ZrSe$_2$ is a semiconductor with an indirect band gap [49–52]. In addition, near the $M(L)$ point, from the ARPES data a bright spectral feature has been noticed at a binding energy of 0.3 eV [shown by red arrow in Fig. 4(c)], which is not predicted from our DFT calculations.
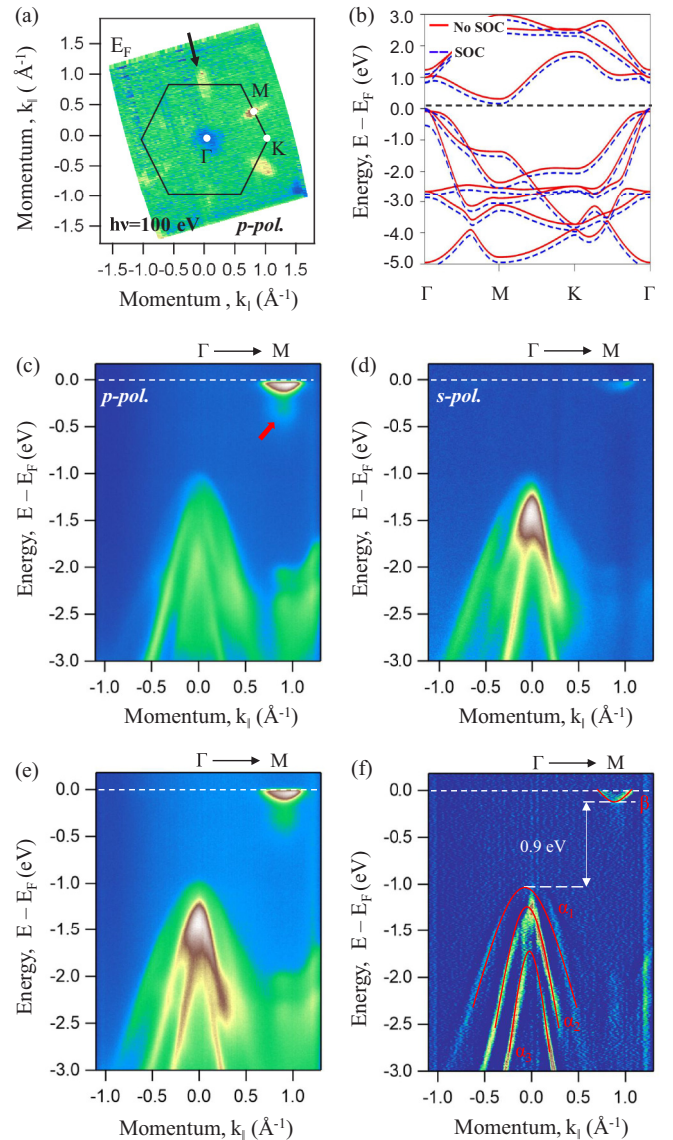
FIG. 4. ARPES spectra of ZrSe$_2$. (a) Fermi surface map measured using p-polarized light with a photon energy of h$\nu = 100$ eV. (b) Energy-momentum plot from the first-principles calculations. (c) EDM cut taken along the direction as shown in (a) measured using p-polarized light. (d) Same as (c) but measured using s-polarized light. (e) Sum of (c) and (d). (f) Second derivative of (e).

However, similar spectral feature has been observed in an earlier ARPES report on ZrSe$_2$ [52].

Top panels in Fig. 5(a) show photon energy dependent EDMs taken along the zone center using s-polarized light. Similarly, bottom panels in Fig. 5(a) show photon energy dependent EDMs taken along the zone center using p-polarized light. Using inner potential of 10.9 eV [50], we identify that 40, 50, 60, and 80 eV photon energies, along Γ-A direction, detect the bands at k_z values of 13.65 $\frac{\pi}{c'}$, 15.05 $\frac{\pi}{c'}$, 16.33 $\frac{\pi}{c'}$, and 18.63 $\frac{\pi}{c'}$. Similarly, in Fig. 5(c), the photon energies 60 and 70 eV, along M-L direction, detect the bands at k_z values of 15.75 $\frac{\pi}{c'}$ and 16.97 $\frac{\pi}{c'}$, respectively. Here, $c' = 2c$ and $c = 6.150$ Å. From the EMDs of both polarizations, we do notice three well resolved hole pockets at the zone center. As
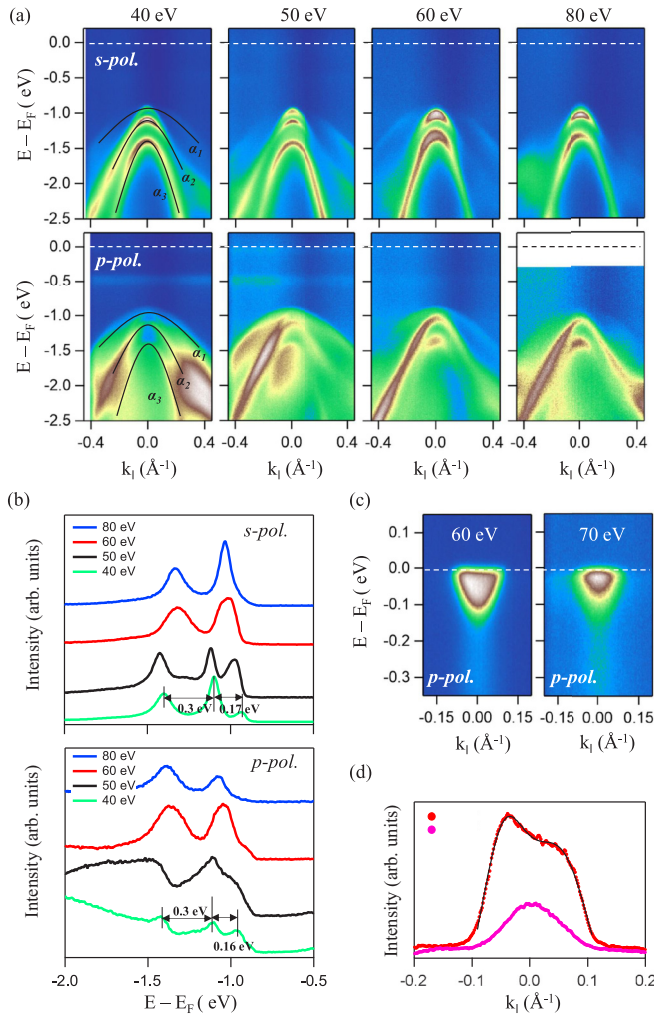
FIG. 5. Photon energy dependent ARPES spectra of ZrSe$_2$. (a) Photon energy dependent EDMs measured using *s*-polarized (top) and *p*-polarized light (bottom) at the zone center. (b) Photon energy dependent EDCs from *s*- and *p*-polarized lights. (c) Photon energy dependent EDMs taken for the electron pocket. (d) Momentum dispersive curves extracted by integrating over 10 meV about the Fermi level, taken from (c).

discussed above, the *p*-polarized light should detect two holelike bands composed of the even parity orbitals p_x and p_z and the *s*-polarized light should detect one holelike band composed of odd parity orbital p_y. However, since the crystal is not oriented in any high-symmetry direction, the photoemission process does not follow the parity dependent selection rules and moreover the orbital contribution to the low-energy band structure of ZrSe$_2$ under SOC is more complex. Hence, we do see all three bands from both *p*- and *s*- polarized lights. Top panel in Fig. 5(b) shows photon energy dependent EDCs taken at $k_\parallel = 0$ from the EDMs of *s*-polarized light. Similarly, bottom panel in Fig. 5(b) shows photon energy dependent EDCs taken at $k_\parallel = 0$ from the EDMs of *p*-polarized light. From the EDCs shown in Fig. 5(b) one can clearly see that the three holelike bands are well separated. For instance, from the EDCs of 40 eV in Fig. 5(b), one peak has been observed at a binding energy of 1.4 eV, corresponding to the top of

holelike band α_3. Another two peaks have been observed at binding energies of 1.1 and 0.93 eV, corresponding to the top of holelike bands α_2 and α_1, respectively. Similar observations were made with 50 eV photon energy. However, when measured with 60 and 80 eV the band separation is not that clear due to either the matrix element effects or k_z dispersion. Figure 5(c) shows EDMs of the electron pocket measured using *p*-polarized light with 60 and 70 eV. Figure 5(d) shows momentum dispersive curves extracted near the Fermi level from the EDMs of Fig. 5(c). From the MDC of 60 eV, we estimated a Fermi vector of $k_F \approx 0.05$ Å^{-1}, while the MDC of 70 eV shows no Fermi vector for the electron pocket. This suggest that the electron pocket composed of Zr d_{z^2} character has significant k_z dispersion in ZrSe$_2$.

V. DISCUSSIONS

Despite sharing the same trigonal crystal structure, the low-energy electronic structures of ZrTe$_2$ and ZrSe$_2$ are clearly differing from one another. ZrTe$_2$ has a metallic band structure with overlapping valance and conduction bands above the Fermi level at the $\Gamma(A)$ point, composed by Te p and Zr d orbitals, respectively. On the other hand, ZrSe$_2$ has a semiconducting nature of the band structure with an indirect band gap of $E_g = 0.9$ eV between $\Gamma(A)$ and $M(L)$ high-symmetry points, with the valance and conduction bands composed of Se p and Zr d orbitals, respectively. In agreement with a previous ARPES report on ZrSe$_2$ [52], a tiny spectral feature near the $M(L)$ point at a binding energy of 0.3 eV has been observed. This feature is more intense when measured with *p*-polarized light than the *s*-polarized light, suggesting that it is composed by an even parity orbital. However, experimentally we are unable to pin point its band dispersion neither to electronlike nor to holelike. Further, this feature is not predicted from the DFT calculations, thus cannot be of the intrinsic origin. As the XPS data of ZrSe$_2$ (see Fig. 1) shows iodine peaks, perhaps, this Iodine impurity could be a plausible source of this strange spectral feature in ZrSe$_2$ than the back-folding of the bands from $M(L)$ to $\Gamma(A)$ as suggested in the Ref. [52]. Moreover, an earlier ARPES study on ZrSe$_2$ showed Fermi level lying in between valence and conduction band [64], whereas from our study, we found that the Fermi level is moved to the conduction band. This could be due to the Se deficiency in ZrSe$_2$ as observed from the EDAX measurements, which is giving rise to the net electron doping.

Spin-orbit coupling seems to be significantly affecting the low-energy electronic structure of these compounds. Especially, in ZrSe$_2$, the DFT calculations without SOC suggest two of the three hole pockets are degenerate, i.e., the two hole pockets composed by p_x and p_y are degenerate while the third hole pocket composed by p_z is well separated from them. The ARPES data of ZrSe$_2$ show three well separated hole pockets near the Γ point. This can only be reproduced in DFT calculations with the inclusion of SOC. In addition, the ARPES data of ZrSe$_2$ suggest a SOC splitting of hole pockets to as high as 0.17 eV. This observation is in very good agreement with the SOC split size of 0.16 eV for the same hole pockets reported by an earlier ARPES study on ZrSe$_2$ [50]. On the other hand, our DFT calculations with SOC only produced a SOC splitting size of 0.085 eV (see Fig. 2).
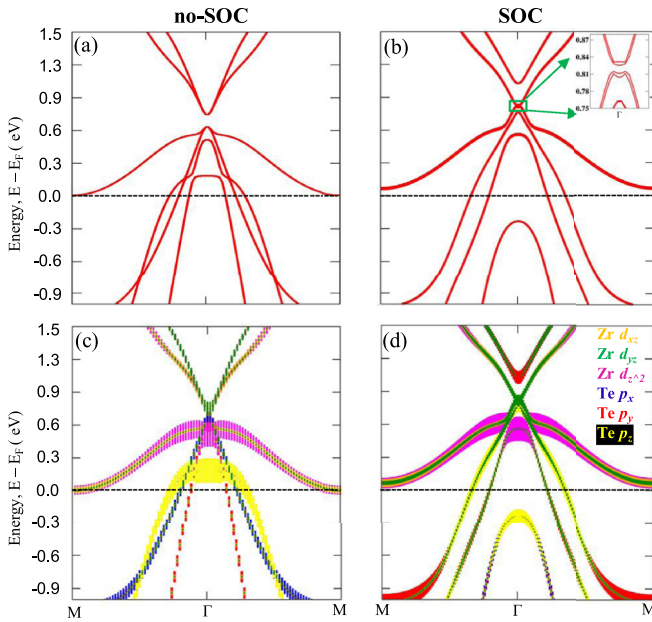
FIG. 6. Calculated band structure of ZrTe$_2$ (a) without SOC and (b) with SOC. (c) and (d) are same as (a) and (b) but with orbital information. Inset in (b) shows a gap of 10 meV opening at the Γ point due to the band inversion under the SOC.

FIG. 7. [(a) and (b)] Energy-momentum plots of ZrSe$_2$ and ZrTe$_2$ obtained form the DFT calculations in the absence of spin-orbit coupling, with overlapped bands derived from the tight-binding (TB) fittings, respectively. (c) Energy-momentum plot of ZrSe$_2$ derived from tight-binding fittings using the on-site energies of ZrTe$_2$. (d) Energy-momentum plot of ZrTe$_2$ derived from tight-binding fittings using the on-site energies of ZeSe$_2$. See Ref. [66] for further details on the on-site energies.

We further would like to show our DFT calculations (see Fig. 6) on ZrTe$_2$ in which we identify a band inversion between Zr d and Te p states at the Γ point. As discussed above, in ZrSe$_2$ a clear separation is noticed between the valence and conduction bands composed by Se p and Zr d states, respectively. In ZrTe$_2$, the Zr d_{z^2} state comes closer to the valence band and in fact touches the valance band at Γ. Further, in the presence of SOC, we clearly observe a band inversion in ZrTe$_2$ in such a way that the Te p_y state moves up to the conduction band, while the Zr d_{z^2} moves further down to the valance band. As a result, a band gap of 10 meV is noticed [see inset in Fig. 6(b)].

Next, coming to the discussion on the electronic structure of ZrTe$_2$, for the first time, we report here the ARPES studies on bulk ZrTe$_2$. An earlier existing the only ARPES study is on monolayer thickness ZrTe$_2$ film deposited on InAs (111), suggesting a Dirac like linear bands at the $\Gamma(A)$ point [56]. Interestingly, our DFT calculations predict a band inversion between Zr d and Te p states at the $\Gamma(A)$ point, hinting at a possible nontrivial band structure in ZrTe$_2$ despite experimentally failing to detect any linear Dirac surface states. Furthermore, with the help of in-plane and out-of-plane ARPES data and Luttinger's theorem [62,63], we calculated the number of hole and electron carriers enclosed by the hole and electron Fermi pockets. Our calculation results to hole carrier density $n_h = 0.003$ per unit cell (1.1×10^{19} cm^{-3}) and electron carriers $n_e = 0.0026$ per unit cell (0.95×10^{19} cm^{-3}). Our estimated electron carrier density value is very close to the value of the order of 10^{19} cm^{-3} reported for Cu$_{0.3}$ZrTe$_{1.2}$ [55], but much higher than the value of 5.07×10^{15} cm^{-3} reported for ZrTe$_2$ [74]. In any case, carrier density reported in Ref. [74] is rather pointing ZrTe$_2$ to a semiconductor, while ZrTe$_2$ is widely known as a metal as

also confirmed by the present study. Equal hole and electron carrier density as derived from our ARPES data in addition to the band inversion as seen from the DFT calculations is suggesting that ZrTe$_2$ is a topological semimetal.

Finally, in order to understand the electronic structure transition from semiconductor to a topological semimetal in going from ZrSe$_2$ to ZrTe$_2$, we mapped the *ab initio* band structure of these systems onto a tight-binding model,

$$\hat{H} = \sum_{i,j} t_{i,j} c_i^\dagger c_j + \sum_i \epsilon_i c_i^\dagger c_i + \text{H.c.} \tag{1}$$

Here, $t_{i,j}$ is the hopping interaction parameter between ith and jth orbitals, and ϵ_i is the on-site energy of orbital i. The charge transfer energy between nth and mth site is given by $\Delta_{i,j}^{n,m} = \epsilon_i^n - \epsilon_j^m$, where $n \neq m$.

The tight-binding model has maximized localized Wannier functions for its radial part. As is evident from Figs. 7(a) and 7(c), we have a good description of the *ab initio* bands. This gives us the confidence in discussing further the changes in the electronic structure in terms of the tight-binding Hamiltonian parameters. As Se is more electronegative than Te, the Se p states are expected to be deeper than the Te p states. This is examined by looking at the charge transfer energy (Δ), defined as $\epsilon_d(\text{Zr}) - \epsilon_p(X)$. Our results of extracted on-site

TABLE I. Tight-binding parameters of MX_2 ($M=$ Zr and Hf; $X=$Se and Te). Here, Δ is the charge transfer energy between transition-metal (M) and chalcogen ion (X). Further detail can be found in Ref. [66].

Composition	Δ (eV)	M-M bond length (Å)	M-X bond length (Å)
$ZrSe_2$	2.282	3.735	2.690
$ZrTe_2$	2.141	3.908	2.894
$HfSe_2$	3.015	2.710	2.660
$HfTe_2$	2.332	3.846	2.856

energies show this trend (see Ref. [66]), with the Δ being smaller by 0.175 eV for $ZrTe_2$ than $ZrSe_2$. Since Zr is in a +4 valence state in these systems, Zr has a d^0 electron count. Consequently, the gap that one finds in these systems is analogous to a bonding-antibonding splitting between the Zr d and X p states.

For the same p-d hopping interaction strength (t) between Zr d and Te p states, the decrease in Δ ingoing from $ZrSe_2$ to $ZrTe_2$ should lead to a larger bonding-antibonding splitting for $ZrTe_2$. This would then lead to a larger band gap for $ZrTe_2$ than that one found in $ZrSe_2$. This is, of course, in contrary to our experimental findings, and the assumption of the similar values of t in the two systems leads to this erroneous conclusion. Moreover, the hopping interaction strengths are expected to scale as $\frac{1}{r^4}$ for p-d interactions, according to the Harrison's empirical law [75]. Here, r is the distance between the Zr and X ions. By examining the crystal structure of $ZrTe_2$ and $ZrSe_2$, we find that the Zr-Te distance (2.894 Å) larger than the Zr-Se distance (2.690 Å). This leads to a smaller t for $ZrTe_2$ compared to $ZrSe_2$. Therefore, in spite of decrease in Δ in $ZrTe_2$, as the smaller t dominates the electronic structure changes, there maybe a smaller bonding-antibonding splitting. Thus $ZrTe_2$ is a semimetal induced by the metal-chalcogen bond length. On the other hand, with the same reasons, the larger t in $ZrSe_2$ makes it semiconducting. Further it should be noted that the relatively larger distances of Zr-Zr, compared to Zr-X (see Table I), seems to be having weaker effect on the electronic structure changes unlike the cases of WTe_2 ($1T'$) and $MoTe_2$ ($1T'$) where the W(Mo)-W(Mo) distance, 2.857 Å (2.899 Å), is very much close to W (Mo)- Te distance, 2.706 Å (2.699 Å).

We then went on further examining to know if this is a generic feature of the compounds from the same column of the periodic table (group IV). For this purpose, we replaced Zr by Hf and performed similar calculations as discussed above. Noteworthy to mention here that the crystal structure of both ZrX_2 and HfX_2 have $1T$ phase. From our calculations, we found similar trends in the bond lengths. That means, Hf-Te bond length is larger than that of Hf-Se (see Table I). Thus $HfTe_2$ has smaller bonding-antibonding splitting compared to $HfSe_2$. This is in good agreement with

the physical properties of $HfSe_2$ and $HfTe_2$, the former is semiconductor with an indirect band gap of 0.9 eV [51] and the later is a semimetal [76]. Thus, similar to ZrX_2, the electronic structure of the Hf compounds also are being determined by the Hf d - X p interactions.

VI. CONCLUSIONS

In conclusion, we systematically studied the low-energy electronic structure of $ZrTe_2$ and $ZrSe_2$ using angle resolved photoemission spectroscopy and density functional theory calculations. ARPES data of $ZrTe_2$ suggest several well disconnected hole and electron pockets at $\Gamma(A)$ and $M(L)$ points, respectively. From the ARPES data of $ZrTe_2$, we realize three holelike nondegenerate band dispersions near the $\Gamma(A)$ point and an electronlike band dispersion at the $M(L)$ point. The experimental observations are in good agreement with the DFT calculations. An equal number of hole and electron carrier density as estimated from our ARPES data suggest $ZrTe_2$ to a semimetal. In addition, the DFT calculations of $ZrTe_2$ in the presence of spin-orbit coupling suggest a band inversion between Te p and Zr d characters near Γ point, hinting $ZrTe_2$ to a topological semimetal. On the other hand, from the Fermi surface topology of $ZrSe_2$, we observe only the electron pockets located at $M(L)$ point, while the hole pockets are noticed well below the Fermi level. Our studies on $ZrSe_2$ further suggest it to a semiconductor with an indirect band gap of 0.9 eV between $\Gamma(A)$ and $M(L)$ high-symmetry points (see Fig. S5 in Ref. [66]). Also, our calculations demonstrate that the metal-chalcogen bond-length plays a vital role on the electronic structure changes of ZrX_2 ($X =$ Se and Te) in such a way that an electronic phase transition takes place from semiconductor to topological semimetal ingoing from $ZrSe_2$ to $ZrTe_2$. This argument is further supported by our systematic calculations performed on another composition (HfX_2) from the same column of the periodic table. That means, the calculations performed on HfX_2 show similar bond length trends while going from $HfSe_2$ to $HfTe_2$.

[1] R. G. Dickinson and L. Pauling, J. Am. Chem. Soc. **45**, 1466 (1923).

[2] J. Wilson and A. Yoffe, Adv. Phys. **18**, 193 (1969).

[3] L. F. Mattheiss, Phys. Rev. B **8**, 3719 (1973).

[4] R. Späh, U. Elrod, M. Lux-Steiner, E. Bucher, and S. Wagner, Appl. Phys. Lett. **43**, 79 (1983).

[5] D. Jiménez, Appl. Phys. Lett. **101**, 243501 (2012).

[6] Q. H. Wang, K. Kalantar-Zadeh, A. Kis, J. N. Coleman, and M. S. Strano, Nat. Nanotech. **7**, 699 (2012).

[7] H. Zeng, J. Dai, W. Yao, D. Xiao, and X. Cui, Nat. Nanotech. **7**, 490 (2012).

[8] R. Cheng, S. Jiang, Y. Chen, Y. Liu, N. Weiss, H.-C. Cheng, H. Wu, Y. Huang, and X. Duan, Nat. Commun. **5**, 5143 (2014).

[9] S. J. Li, J. C. Bernède, J. Pouzet, and M. Jamali, J. Phys.: Condens. Matter **8**, 2291 (1996).

[10] M. S. Fuhrer and J. Hone, Nat. Nanotechnol. **8**, 146 (2013).

[11] W. Wu, L. Wang, Y. Li, F. Zhang, L. Lin, S. Niu, D. Chenet, X. Zhang, Y. Hao, T. F. Heinz, J. Hone, and Z. L. Wang, Nature (London) **514**, 470 (2014).

[12] C. Gong, Y. Zhang, W. Chen, J. Chu, T. Lei, J. Pu, L. Dai, C. Wu, Y. Cheng, T. Zhai, L. Li, and J. Xiong, Adv. Sci. **4**, 1700231 (2017).

[13] M. Khan and M. N. Leuenberger, Nanophotonics **7**, 1589 (2018).

[14] A. T. Neal, Y. Du, H. Liu, and P. D. Ye, ACS Nano **8**, 9137 (2014).

[15] Z. Zhang, J. Niu, P. Yang, Y. Gong, Q. Ji, J. Shi, Q. Fang, S. Jiang, H. Li, X. Zhou, L. Gu, X. Wu, and Y. Zhang, Adv. Mater. **29**, 1702359 (2017).

[16] J. Zhang, B. Yang, H. Zheng, X. Han, and Y. Yan, Phys. Chem. Chem. Phys. **19**, 24341 (2017).

[17] M. N. Ali, J. Xiong, S. Flynn, J. Tao, Q. D. Gibson, L. M. Schoop, T. Liang, N. Haldolaarachchige, M. Hirschberger, N. P. Ong, and R. J. Cava, Nature (London) **514**, 205 (2014).

[18] J. Jiang, Z. Liu, Y. Sun, H. Yang, C. Rajamathi, Y. Qi, L. Yang, C. Chen, H. Peng, C.-C. Hwang, S. Sun, S.-K. Mo, I. Vobornik, J. Fujii, S. Parkin, C. Felser, B. Yan, and Y. Chen, Nat. Commun. **8**, 13973 (2017).

[19] S. Thirupathaiah, R. Jha, B. Pal, J. S. Matias, P. K. Das, P. K. Sivakumar, I. Vobornik, N. C. Plumb, M. Shi, R. A. Ribeiro, and D. D. Sarma, Phys. Rev. B **95**, 241105(R) (2017).

[20] H. Ma, P. Chen, B. Li, J. Li, R. Ai, Z. Zhang, G. Sun, K. Yao, Z. Lin, B. Zhao, R. Wu, X. Tang, X. Duan, and X. Duan, Nano Lett. **18**, 3523 (2018).

[21] X. guaug Zheng, H. Kuriyaki, and K. Hirakawa, J. Phys. Soc. Jpn. **58**, 622 (1989).

[22] Y.-C. Lin, D. O. Dumcenco, Y.-S. Huang, and K. Suenaga, Nat. Nanotechnol. **9**, 391 (2014).

[23] H. M. Hill, A. F. Rigosi, K. T. Rim, G. W. Flynn, and T. F. Heinz, Nano Lett. **16**, 4831 (2016).

[24] M. Salavati, Front. Struct. Civ. Eng. **13**, 486 (2018).

[25] T. Pillo, J. Hayoz, H. Berger, R. Fasel, L. Schlapbach, and P. Aebi, Phys. Rev. B **62**, 4277 (2000).

[26] L. Perfetti, P. A. Loukakos, M. Lisowski, U. Bovensiepen, H. Berger, S. Biermann, P. S. Cornaglia, A. Georges, and M. Wolf, Phys. Rev. Lett. **97**, 067402 (2006).

[27] C. Zhang, S. KC, Y. Nie, C. Liang, W. G. Vandenberghe, R. C. Longo, Y. Zheng, F. Kong, S. Hong, R. M. Wallace, and K. Cho, ACS Nano **10**, 7370 (2016).

[28] K. F. Mak, C. Lee, J. Hone, J. Shan, and T. F. Heinz, Phys. Rev. Lett. **105**, 136805 (2010).

[29] A. Kumar and P. K. Ahluwalia, Eur. Phys. J. B **85**, 186 (2012).

[30] W. Choi, N. Choudhary, G. H. Han, J. Park, D. Akinwande, and Y. H. Lee, Mater. Today **20**, 116 (2017).

[31] M. Porer, U. Leierseder, J.-M. Ménard, H. Dachraoui, L. Mouchliadis, I. E. Perakis, U. Heinzmann, J. Demsar, K. Rossnagel, and R. Huber, Nat. Mater. **13**, 857 (2014).

[32] L. J. Li, W. J. Zhao, B. Liu, T. H. Ren, G. Eda, and K. P. Loh, Appl. Phys. Lett. **109**, 141902 (2016).

[33] Y. Ma, Y. Dai, M. Guo, C. Niu, Y. Zhu, and B. Huang, ACS Nano **6**, 1695 (2012).

[34] X. Zhu, Y. Guo, H. Cheng, J. Dai, X. An, J. Zhao, K. Tian, S. Wei, X. C. Zeng, C. Wu, and Y. Xie, Nat. Commun. **7**, 11210 (2016).

[35] H. Xiang, B. Xu, Y. Xia, J. Yin, and Z. Liu, Sci. Rep. **6**, 39218 (2016).

[36] Y. I. Joe, X. M. Chen, P. Ghaemi, K. D. Finkelstein, G. A. de la Peña, Y. Gan, J. C. T. Lee, S. Yuan, J. Geck, G. J. MacDougall, T. C. Chiang, S. L. Cooper, E. Fradkin, and P. Abbamonte, Nat. Phys. **10**, 421 (2014).

[37] C.-X. Liu, Phys. Rev. Lett. **118**, 087001 (2017).

[38] S. C. de la Barrera, M. R. Sinko, D. P. Gopalan, N. Sivadas, K. L. Seyler, K. Watanabe, T. Taniguchi, A. W. Tsen, X. Xu, D. Xiao, and B. M. Hunt, Nat. Commun. **9**, 1427 (2018).

[39] A. Ramasubramaniam, D. Naveh, and E. Towe, Phys. Rev. B **84**, 205325 (2011).

[40] R. Das, B. Rakshit, S. Debnath, and P. Mahadevan, Phys. Rev. B **89**, 115201 (2014).

[41] H. C. P. Movva, T. Lovorn, B. Fallahazad, S. Larentis, K. Kim, T. Taniguchi, K. Watanabe, S. K. Banerjee, A. H. MacDonald, and E. Tutuc, Phys. Rev. Lett. **120**, 107703 (2018).

[42] M. Aghajanian, A. A. Mostofi, and J. Lischner, Sci. Rep. **8**, 13611 (2018).

[43] H. Guo, N. Lu, L. Wang, X. Wu, and X. C. Zeng, J. Phys. Chem. C **118**, 7242 (2014).

[44] L. ping Feng, N. Li, M. hao Yang, and Z. tang Liu, Mater. Res. Bull. **50**, 503 (2014).

[45] M. Yi, D. Lu, J.-H. Chu, J. G. Analytis, A. P. Sorini, A. F. Kemper, B. Moritz, S.-K. Mo, R. G. Moore, M. Hashimoto, W.-S. Lee, Z. Hussain, T. P. Devereaux, I. R. Fisher, and Z.-X. Shen, Proc. Natl. Acad. Sci. **108**, 6878 (2011).

[46] Y. Zhang, C. He, Z. R. Ye, J. Jiang, F. Chen, M. Xu, Q. Q. Ge, B. P. Xie, J. Wei, M. Aeschlimann, X. Y. Cui, M. Shi, J. P. Hu, and D. L. Feng, Phys. Rev. B **85**, 085121 (2012).

[47] S. Thirupathaiah, E. D. L. Rienks, H. S. Jeevan, R. Ovsyannikov, E. Slooten, J. Kaas, E. van Heumen, S. de Jong, H. A. Dürr, K. Siemensmeyer, R. Follath, P. Gegenwart, M. S. Golden, and J. Fink, Phys. Rev. B **84**, 014531 (2011).

[48] H. E. Brauer, H. I. Starnberg, L. J. Holleboom, and H. P. Hughes, J. Phys.: Condens. Matter **7**, 7741 (1995).

[49] M. Moustafa, T. Zandt, C. Janowitz, and R. Manzke, Phys. Rev. B **80**, 035206 (2009).

[50] M. Moustafa, A. Ghafari, A. Paulheim, C. Janowitz, and R. Manzke, J. Electron Spectrosc. Relat. Phenom. **189**, 35 (2013).

[51] M. J. Mleczko, C. Zhang, H. R. Lee, H.-H. Kuo, B. Magyari-Köpe, R. G. Moore, Z.-X. Shen, I. R. Fisher, Y. Nishi, and E. Pop, Sci. Adv. **3**, e1700481 (2017).

[52] A. Ghafari, M. Moustafa, G. D. Santo, L. Petaccia, and C. Janowitz, Appl. Phys. Lett. **112**, 182105 (2018).

[53] A. H. Reshak and S. Auluck, Physica B **353**, 230 (2004).

[54] A. Kumar, H. He, R. Pandey, P. K. Ahluwalia, and K. Tankeshwar, Phys. Chem. Chem. Phys. **17**, 19215 (2015).

[55] A. J. S. Machado, N. P. Baptista, B. S. de Lima, N. Chaia, T. W. Grant, L. E. Corrêa, S. T. Renosto, A. C. Scaramussa, R. F.

Jardim, M. S. Torikachvili, J. A. Aguiar, O. C. Cigarroa, L. T. F. Eleno, and Z. Fisk, Phys. Rev. B **95**, 144505 (2017).

[56] P. Tsipas, D. Tsoutsou, S. Fragkos, R. Sant, C. Alvarez, H. Okuno, G. Renaud, R. Alcotte, T. Baron, and A. Dimoulas, ACS Nano **12**, 1696 (2018).

[57] M. H. Whangbo, F. J. DiSalvo, and R. M. Fleming, Phys. Rev. B **26**, 687 (1982).

[58] G. Manzoni, L. Gragnaniello, G. Autès, T. Kuhn, A. Sterzi, F. Cilento, M. Zacchigna, V. Enenkel, I. Vobornik, L. Barba, F. Bisti, P. Bugnon, A. Magrez, V. N. Strocov, H. Berger, O. V. Yazyev, M. Fonin, F. Parmigiani, and A. Crepaldi, Phys. Rev. Lett. **117**, 237601 (2016).

[59] Y. Zhang, C. Wang, L. Yu, G. Liu, A. Liang, J. Huang, S. Nie, X. Sun, Y. Zhang, B. Shen, J. Liu, H. Weng, L. Zhao, G. Chen, X. Jia, C. Hu, Y. Ding, W. Zhao, Q. Gao, C. Li, S. He, L. Zhao, F. Zhang, S. Zhang, F. Yang, Z. Wang, Q. Peng, X. Dai, Z. Fang, Z. Xu, C. Chen, and X. J. Zhou, Nat. Commun. **8**, 15512 (2017).

[60] L. Shen, M. Wang, S. Sun, J. Jiang, X. Xu, T. Zhang, Q. Zhang, Y. Lv, S. Yao, Y. Chen, M. Lu, Y. Chen, C. Felser, B. Yan, Z. Liu, L. Yang, and Y. Chen, J. Electron Spectrosc. Relat. Phenom. **219**, 45 (2017).

[61] H. Xiong, J. A. Sobota, S.-L. Yang, H. Soifer, A. Gauthier, M.-H. Lu, Y.-Y. Lv, S.-H. Yao, D. Lu, M. Hashimoto, P. S. Kirchmann, Y.-F. Chen, and Z.-X. Shen, Phys. Rev. B **95**, 195119 (2017).

[62] J. M. Luttinger, Phys. Rev. **119**, 1153 (1960).

[63] M. Oshikawa, Phys. Rev. Lett. **84**, 3370 (2000).

[64] K. Nikonov, N. Ehlen, B. Senkovskiy, N. Saigal, A. Fedorov, A. Nefedov, C. Wöll, G. D. Santo, L. Petaccia, and A. Grüneis, Dalton Trans. **47**, 2986 (2018).

[65] H. Schäfer, *Chemical Transport Reactions* (Academic Press, New York, 1964).

[66] See Supplemental Material at http://link.aps.org/supplemental/ 10.1103/PhysRevB.101.165122 for additional DFT calculations, ARPES data, and EDAX analysis on ZrX_2 (X = Se and Te).

[67] S. V. Borisenko, Synchrotron Radiation News **25**, 6 (2012).

[68] S. V. Borisenko, V. B. Zabolotnyy, D. V. Evtushinsky, T. K. Kim, I. V. Morozov, A. N. Yaresko, A. A. Kordyuk, G. Behr, A. Vasiliev, R. Follath, and B. Büchner, J. Vis. Exp. **68**, e50129 (2012).

[69] G. Kresse and J. Furthmüller, Phys. Rev. B **54**, 11169 (1996).

[70] G. Kresse and D. Joubert, Phys. Rev. B **59**, 1758 (1999).

[71] J. P. Perdew, K. Burke, and M. Ernzerhof, Phys. Rev. Lett. **77**, 3865 (1996).

[72] A. A. Mostofi, J. R. Yates, Y.-S. Lee, I. Souza, D. Vanderbilt, and N. Marzari, Comput. Phys. Commun. **178**, 685 (2008).

[73] C. Franchini, R. Kováčik, M. Marsman, S. S. Murthy, J. He, C. Ederer, and G. Kresse, J. Phys.: Condens. Matter **24**, 235602 (2012).

[74] D. N. Bhavsar, A. K. Dasadia, B. B. Nariya, M. K. Bhayani, and A. R. Jani, in *Solid State Physics, Proceeding of the 55th Dae Solid State Physics Symposium 2010*, edited by Alka B. Garg, R. Mittal, and R. Mukhopadhyay, AIP Conf. Proc. No. 1349 (AIP, New York, 2011), p. 1085.

[75] W. A. Harrison, *Electronic Structure and the Properties of Solids: The Physics of the Chemical Bond* (Dover, New York, USA, 1967).

[76] S. Mangelsen, P. G. Naumov, O. I. Barkalov, S. A. Medvedev, W. Schnelle, M. Bobnar, S. Mankovsky, S. Polesya, C. Näther, H. Ebert, and W. Bensch, Phys. Rev. B **96**, 205148 (2017).